Journal Pre-proofs

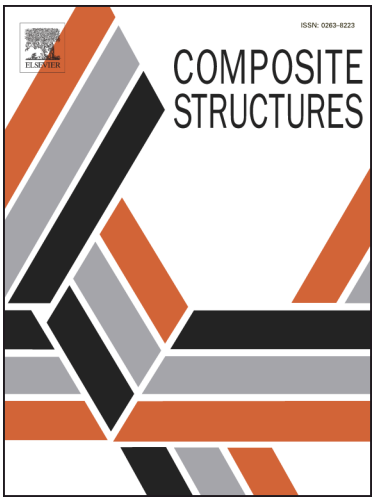

Shape Optimisation and Buckling Analysis of Large Strain Zero Poisson's Ratio Fish-Cells Metamaterial for Morphing Structures

Ashutosh Jha, Iman Dayyani

PII: S0263-8223(21)00455-4
DOI: https://doi.org/10.1016/j.compstruct.2021.113995
Reference: COST 113995

To appear in: *Composite Structures*

Received Date: 14 December 2020
Accepted Date: 13 April 2021

Please cite this article as: Jha, A., Dayyani, I., Shape Optimisation and Buckling Analysis of Large Strain Zero Poisson's Ratio Fish-Cells Metamaterial for Morphing Structures, *Composite Structures* (2021), doi: https://doi.org/10.1016/j.compstruct.2021.113995

Composite Structures, Volume 268, July 2021, Article number 113995
DOI:10.1016/j.compstruct.2021.113995

Shape Optimisation and Buckling Analysis of Large Strain Zero Poisson's Ratio Fish-Cells Metamaterial for Morphing Structures

Ashutosh Jha, Iman Dayyani*

* Corresponding Author: Dr Iman Dayyani
Email: I.Dayyani@Cranfield.ac.uk

Centre for Structures, Assembly, and Intelligent Automation
Cranfield University, MK43 0AL, UK

GRAPHICAL ABSTRACT

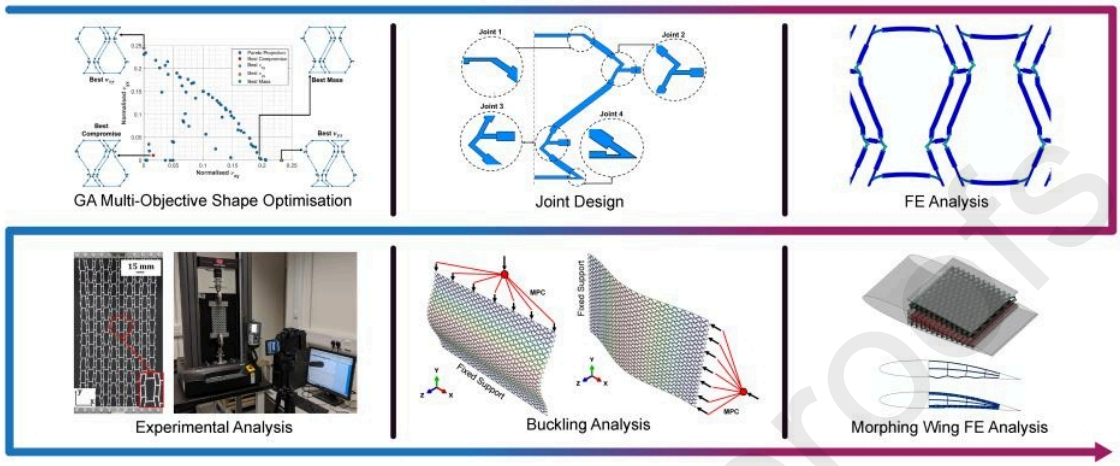

ABSTRACT

This article investigates the potential of a large strain morphing skin based on a Zero Poisson's Ratio (ZPR) Fish-Cells metamaterial. A multi-objective genetic algorithm shape optimisation is performed to improve the ZPR characteristics of the Fish-Cells metamaterial. High-fidelity finite element models are developed to assess the performance of the optimised Fish-Cells metamaterial for large non-linear strains. A detailed joint design study is devised to obtain consistent ZPR behaviour over a maximum strain range. Trends of Poisson's ratio, effective elastic modulus and von-mises stress for the different geometries are discussed in detail. Results provide valuable insight into non-linear behaviour of the Fish-Cells ZPR metamaterial. Furthermore, experimental investigations are conducted to verify the enhanced mechanical behaviour of shape optimised ZPR samples. Linear buckling analysis is performed to assess the performance of the optimised metamaterial under compressive loads. Finally, a preliminary study is conducted to evaluate the performance of the shape optimised ZPR metamaterial as a candidate skin for a morphing aircraft wing.

Keywords:
Multi-Objective Shape Optimisation; Large Strain Zero Poisson's Ratio (ZPR) Mechanical Metamaterials; Joint Design; Experimental Investigation; Buckling Analysis; Morphing Skin

1 Introduction

1.1 Morphing Structures

Morphing structures as biologically inspired designs have an intelligent ability to optimise their shape in operation using distributed sensors and actuators. The radical continuous aerodynamic shape change attained by morphing technology enhances the flow control effectiveness and offers significant improvements in aircraft performance [1]. This is in light of the active evolution of smart structure technology, which has attracted significant interest from global researchers and investors. The multidisciplinary nature of these structures has generated a non-trivial impact on the control of vibrations, noise, and structural integrity. Their applications have a diverse range from aircraft to automobile structure, wind turbine and robotics [2–6]. The current state-of-the-art morphing technologies consist of a complex web of mechanisms constructed from high stiffness materials usually coupled with a hydraulic/pneumatic actuation systems [7]. Researchers have identified penalties in the form of excessive cost, reliability, and complexity of the current morphing technology. Some suggested solutions are based on the integration of the structure with the actuation system using smart materials [2,8].

However, the requirements for morphing structures are conflicting; the structure must be stiff to withstand the external loads and flexible enough to enable shape changes. The solution to this conflict is to design the

structure to decouple the two actions through components with extreme anisotropy and integrated actuation without having a negative impact on the weight, complexity, and reliability of morphing systems. This requires unconventional material characteristics which are achieved based on a bio-inspired philosophy, where many levels of hierarchy in the multiscale structural design are used to improve material performance and functionality. Introducing hierarchy into morphing technology can be achieved through the integration of metamaterials and morphing structures which allows the adaptation and optimization of the material for outstanding performance.

1.2 Mechanical Metamaterials

Metamaterials are artificially structured materials with exceptional physical properties, notably in mechanics, electromagnetics, optics, and acoustics. They are made from assembling multiple elements forming a unit cell in small-scale, which is then periodically repeated over a large-scale. Their exotic properties are derived from the properties of the constituent materials as well as the precise geometry and tessellation of the unit cell. Recent manufacturing technologies of nano/microstructures have been attracting attention increasingly to mechanical metamaterials [9,10]. Based on Poisson's ratio, mechanical metamaterials can be classified into Positive Poisson's Ratio (PPR), Negative Poisson's ratio (NPR) or auxetics and Zero Poisson's Ratio (ZPR) metamaterials [11–13]. Grima et al. have compared the performance of PPR, NPR and ZPR metamaterials in the context of geometric conformability over curved surfaces [11]. The authors state that the ZPR metamaterial shows high integrity and potential for out-of-plane morphing due to its tendency to show unclastic curvature.

In the context of large strain ZPR metamaterials, the need is to have a constant zero Poisson's ratio behaviour over a large strain range for morphing applications being affected by tessellation geometry, deformation mechanism and original constituent material. Ren et al. developed an elastomer skin that showed ZPR behaviour for up to 25% strain which was limited by the ultimate strain of the elastomer material. The mechanism employed pure tensile stretching as its inherent deformation mechanism [14]. Liu et al. introduced a filamentary microstructure with the aim to maximise the strain range of the soft network materials. They reported constant ZPR behaviour for up to a strain range of 60% [15]. Yang and Ma proposed 2D architected mechanical metamaterials whose tensile mechanical response can be tailored by harnessing snap-through instabilities. Based on their 2D double-U architecture, a 3D ZPR mechanical metamaterial was developed which exhibited ZPR behaviour for up to 200% and 67% under tension and compression, respectively [16].

1.3 Maximising the Strain Range of Poisson Ratio Mechanical Metamaterials

There are limited studies available on mechanisms for maximising strain range with constant ZPR behaviour. Adjusting the deformation mechanism can improve and potentially extends the range of ZPR deformations that a metamaterial has due to the inherent unit cell architecture [25]. However, the methodologies used for large strain NPR may be applied to ZPR metamaterials. For example, Chang et al. [17] and Liu et al. [18] reviewed the effects of geometry changes on auxetic structures. They observed that auxetic behaviour is a function of change in the angle between the members of the unit cell as it deforms. Although the unit cell introduces structural weak points at the joints, they reported that reducing the joint thickness makes the structure more stretchable. To solve this, Ebrahimi et al. [17] explored the possibility of using different materials with lower stiffness at the joints using hybrid material 3D printing technology, hence, they obtained higher stretching capacity of the auxetic structure without reducing the thickness at the joints.

Structural optimisation of the auxetic tessellation and local joints was another way to extend the strain range for auxetics in literature, for example, Clausen et al. achieved a constant negative Poisson's ratio over a strain range of 20% with topology optimisation techniques [19]. Also, Ebrahimi et al. introduced chiral hinges at the joints of their design to achieve a consistent NPR over a strain range of 25% [23]. Ge et al. [20] investigated mainly the auxetic behaviour of textile structures for composite reinforcement using three different yarn systems. Also, they observed a constant ZPR behaviour for up to 40% strain under compression by parameterising the spacing between the two yarns and the initial radius of the yarns.

Metamaterials mentioned above exhibit ZPR behaviour only up to a critical strain usually limited by the joint rotations and relative deformations of slender elements of the unit cell. Also, from a structural

integrity perspective, the existing large strain tessellation shows unreliable behaviour such as critical stress for practical applications (e.g. morphing wing). Nearly no literature use shape optimisation and detailed joint design of unit-cell architecture to improve and sustain ZPR characteristic over a large strain.

This article optimises the shape and investigates the joint design of Fish-Cells ZPR metamaterials [21] for large deformations. Genetic algorithm multi-objective optimisation is performed to minimise the mass and ZPR in longitudinal-y and transverse-x directions of loading. In this regard, a finite element code to simulate a Fish-Cells ZPR metamaterial under tensile loading is developed in MATLAB using 2D beam elements. In addition, high-fidelity FE models are generated in ABAQUS assessing the design objectives for large nonlinear deformations. Detailed parametric joint design analysis is performed to sustained ZPR behaviour for large strains. Experimental investigations are conducted to verify the enhanced mechanical behaviour of shape optimised ZPR metamaterials. Linear buckling analysis is performed to assess the performance of the optimised metamaterial under compressive loads. This especially important in the case of morphing wing as out of the top and the bottom morphing panels of the wing, one will always be in tension the other in compression. Thus, understanding the buckling behaviour of the morphing panel under compression becomes a critical parameter for consideration in the case of morphing wing design. Also, this is the first time the buckling behaviour of planar ZPR metamaterial has been considered. Finally, the performance of the optimised Fish-Cells metamaterial is evaluated as a candidate for morphing skin with different out-of-plane panel thickness.

2 Problem Formulation

Naghavi Zadeh et al. introduced a new metamaterial called Fish-Cells which shows ZPR in two planar directions for linear elastic strain [18]. Further in the article, the geometry is referred to as baseline, which does not maintain ZPR over large strains and is not ideal for morphing application (such as morphing aircraft wing). In this article, the shape of the Fish-Cells is optimised by introducing new points in the Fish-Cells configuration and a multi-objective optimisation is performed by minimising the Poisson's ratio in the longitudinal-y and transverse-x direction while minimising the mass of the skin.

2.1 Material Characterisation

Five dog-bone tensile test samples were manufactured using an Ultimaker 2^+ 3D printer with Polylactic Acid (PLA). The dog-bone samples were then tested in accordance with the ASTM D638-14 standard. These tests were performed using an Instrom 5965 tensile test machine using a 5kN load cell. The stress-strain curves for the dog bone samples are illustrated in Fig. 1, from where the average value of the elastic properties and the plastic stress-strain data are calculated as described in Table 1. It must be noted that plasticity was only considered for the experimental analysis and not for the optimisation and joint design analysis.

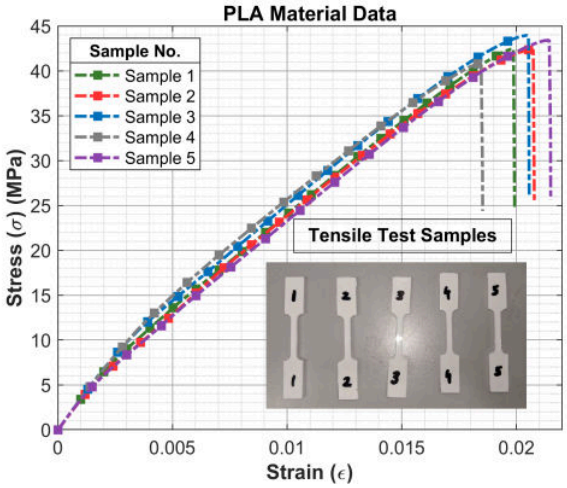

Fig. 1: Stress-strain data for five PLA dog bone test samples.

Table 1: PLA elastic material properties and plastic stress-strain data.

Elastic Material Properties	
Elastic Modulus (E)	1700 MPa
Yield Stress (σ_y)	22 MPa
Ultimate Stress (σ_{ut})	43 MPa
Poisson's Ratio (ν)	0.36

Plastic Material Properties for Experimental Validations	
Strain [mm/mm]	Stress [MPa]
0.0000	22.0285
0.0160	22.2480
0.0200	25.7206
0.0250	29.5356
0.0300	33.0714
0.0350	36.6431
0.0400	40.0944
0.0451	43.5350

2.2 Finite Element Programming for Shape Optimisation

A 2D FE code based on thin beams with cubic shape function is developed in MATLAB for evaluation of the Poisson' ratios and mass fitness functions. Figure Fig. 2 shows the domain of the baseline Fish-Cells identified by basic nodes with fixed coordinates as described in Table 2. Also, 24 non-basic nodes are introduced in the geometry of the unit cell as optimisation parameters. The distribution of two non-basic nodes per inclined members is limited by the mass of the structure, manufacturing constraints and computation time.

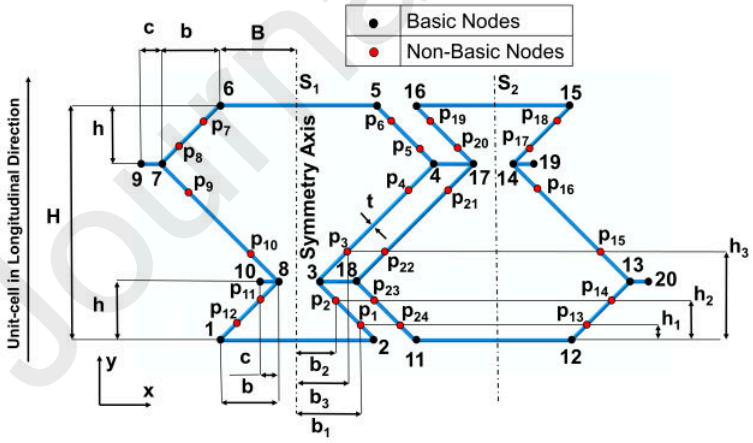

Fig. 2: Geometry of the unit Fish-Cells describing the locations of the fixed nodes (basic nodes in black) and optimisation nodes (non-basic nodes in red).

Table 2: Parameters and dimensions of the baseline Fish-Cells [21].

Parameter	**Dimension [mm]**
B	8
H	24
b	6
h	6
c	2
t	1
w	1.5

As illustrated in Fig. 2, the non-basic nodes p_1 to p_{24} contain the x and y coordinates of each node. i.e.

$$p_n = (x_n, y_n);\ n \in [1,24];\ n \in \mathbf{N};\ x_n, y_n \in \mathbf{R} \quad (1)$$

Naghavi Zadeh et al. observed that for an arbitrary Fish-Cells topology to exhibit ZPR behaviour, the non-basic nodes p_1, p_2, p_3 must be point symmetric with the nodes p_6, p_5 and p_4, respectively, about the mid-point of member $\overline{34}$ [23]. i.e.

$$p_4\begin{cases}x_4 = 2B - x_3\\ y_4 = H - y_3\end{cases}$$
$$p_5\begin{cases}x_5 = 2B - x_2\\ y_5 = H - y_2\end{cases} \quad (2)$$
$$p_6\begin{cases}x_4 = 2B - x_1\\ y_4 = H - y_1\end{cases}$$

Non-basic nodes p_7, p_8, p_9, p_{10}, p_{11}, p_{12} are symmetric to non-basic nodes p_6, p_5, p_4, p_3, p_2, p_1, respectively, about the symmetry axis S_1, as illustrated in Fig. 2. Furthermore, the positions of the remaining nodes can be calculated using periodicity. Hence, the coordinates of the non-basic nodes p_1, p_2, and p_3 are considered for the optimisation process.

Figure Fig. 3 illustrates the tessellation of the unit cell, with the rectangular domain positioned at the centre of the metamaterial to measure the Poisson's ratio where the boundary conditions effects are minimised [18]. The boundary conditions are described for every edge for both the directions of tensile loading in Table 3. The FE code was validated using an identical model developed in ABAQUS. The nodal displacements were measured and compared at four points of the rectangular domain (A, B, C and D). A maximum deviation of 0.01% was recorded, which is well within an acceptable tolerance.

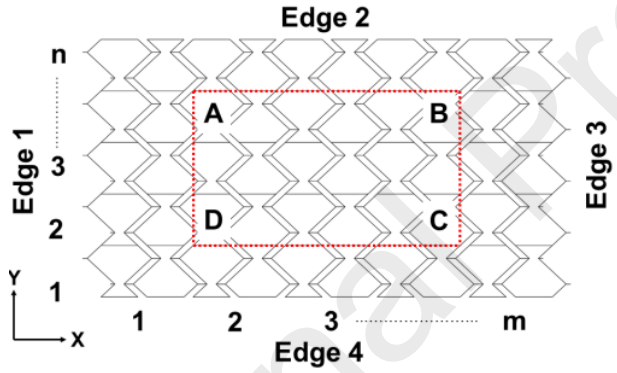

Fig. 3: Planar tessellation with edge annotations and rectangular domain (ABCD) used for measuring Poisson's ratio.

Table 3: Boundary conditions for simulating tensile test in longitudinal-y and transverse-x directions of loading (edges described in Fig. 3).

Edge	Direction of Tensile Loading: Longitudinal y	Direction of Tensile Loading: Transverse x
1	Free	$\varepsilon_x = 0$ $\varepsilon_y = 0$ $UR_3 = 0$
2	$\varepsilon_x = 0$ $\varepsilon_y = 0.01$ $UR_3 = 0$	Free
3	Free	$\varepsilon_x = 0.01$ $\varepsilon_y = 0$ $UR_3 = 0$
4	$\varepsilon_x = 0$ $\varepsilon_y = 0$ $UR_3 = 0$	Free

2.3 Genetic Algorithm Multi-Objective Shape Optimisation

The FE code developed in section 2.2 is used in conjunction with a multi-objective genetic algorithm optimisation toolbox in MATLAB. The following three objectives are defined for the minimisation problem:

- ν_{yx}: Poisson's ratio of metamaterial under tensile loading in the longitudinal-y direction
- ν_{xy}: Poisson's ratio of metamaterial under tensile loading in the transverse-x direction
- Mass: Total mass of the metamaterial

To call for the best performance from the selected optimisation scheme, the variables and the objective functions are normalised using Equation (3) and Equation (4), respectively [24].

$$x_n(i) = \frac{\left(x(i) - \left(\frac{x_u(i) - x_l(i)}{2}\right)\right)}{\left(\frac{x_u(i) - x_l(i)}{2}\right)}; i \in [1,6];\ i \in \mathbf{Z};\ ;\ x_l(i), x_u(i), x(i) \in \mathbf{R} \tag{3}$$

where x is the vector parameter, x_u is the lower bound and x_l is the upper bound

$$f_n(x) = f(x)/f(\bar{x})$$
$$\bar{x} = \frac{x_u + x_l}{2} \tag{4}$$

In which $\bar{x}$ is the average vector of the upper (x_u) and the lower (x_l) bounds. The upper and the lower bounds for the six corresponding variables considered in the optimisation are described in Equation (5). These upper and the lower bounds for the variables are selected to avoid potential contact or overlap between two adjacent members of the Fish-Cells.

$$p_1 = \begin{cases} x_1 ; where\ x_1 \in [0,B] \\ y_1 ; where\ y_1 \in [0,0.5\mathrm{H}] \end{cases}$$
$$p_2 = \begin{cases} x_2 ; where\ x_2 \in [0,B] \\ y_2 ; where\ y_2 \in [0,0.5\mathrm{H}] \end{cases} \quad \text{where } x_1, x_2, x_3, y_1, y_2, y_3 \in \mathbf{R} \tag{5}$$
$$p_3 = \begin{cases} x_3 ; where\ x_3 \in [0,B] \\ y_3 ; where\ y_3 \in [0,0.5\mathrm{H}] \end{cases}$$

A tessellation size of 5x5 is selected for the optimisation process due to the limitation of computational resources. A tessellation of 5x5 consisted of 980 nodes with 3 degrees of freedoms, resulting in the stiffness matrix size of 2940x2940. A crossover fraction of 0.3 was selected as it produces minimum deviation for each objective function, as demonstrated by Dayyani et al. [25], Ermakova et al. [26] and Lim et al. [27]. The computation was performed on a system equipped with a 16-Core Intel E5 – 2660 processor with a total of 128GB RAM. The results were obtained for the optimisation process for population sizes of 100, 200 and 400. It is observed that a population size of 200 provided an acceptable balance between computational efficiency and effectiveness of the optimisation process. The results for the optimisation process are discussed in detail in the next section.

3 Shape Optimisation Results

3.1 Optimisation Results

Figure Fig. 4a illustrates the normalised 3D Pareto and their projection plot obtained from the optimisation process. The point closest to the origin is considered as the best compromise and is marked in red [28]. Figure Fig. 4b illustrates the different optimised shapes of the unit cells at dominant single objective function points including best ν_{yx}, best ν_{xy}, best mass and best compromise point. Table 4 describes the dimension of the unit cell at these four points along with their function values. It must be noted that the geometric parameters defined in Table 4 are only valid for a domain with a B/H ratio and b/h ratio of 0.33 and 1, respectively. A nominal variation of normalised mass is observed, relative to ν_{yx} and ν_{xy}. Comparing the lightest and the heaviest shapes, a maximum variation of 35% is identified. The best compromise Fish-Cells metamaterial is selected for further study as it shows potential for ZPR morphing application in the longitudinal-y and transverse-x direction while having small mass. The best compromise Fish-Cells metamaterial is denoted as the optimised metamaterial for the rest of this article.

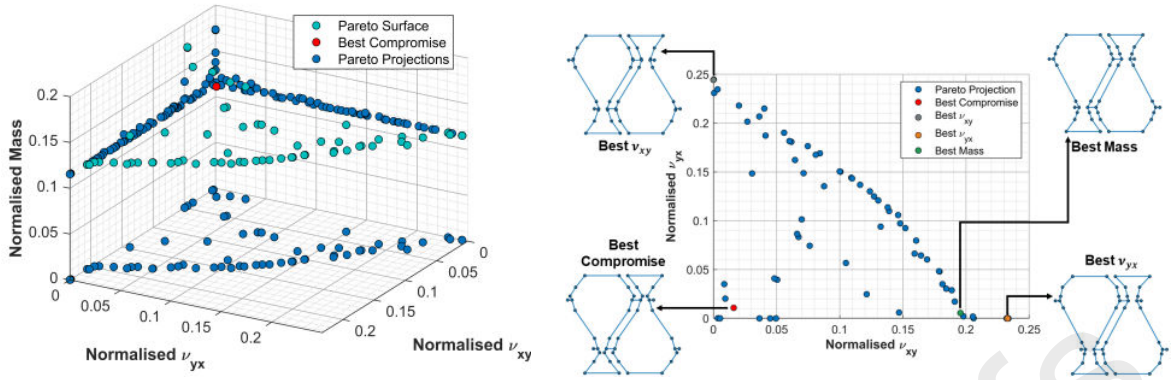

(a) (b)

Fig. 4: Results obtained from the optimisation process (a) Pareto surface in 3D space (in teal) and their projections (in blue) on corresponding planes along with the best compromise point (red); (b) Pareto projection showing normalised ν_{yx} vs ν_{xy} illustrating the geometry of the Fish-Cells obtained at best ν_{yx}, best ν_{xy}, best mass and best compromise points.

Table 4: Dimensions and function values of the shape optimised Fish-Cells metamaterial

		Optimised Geometry			
Parameters		**Best Compromise**	**Best ν_{yx}**	**Best ν_{xy}**	**Best Mass**
p_1	b_1	0.47 B	0.25 B	0.49 B	0.50 B
	h_1	0.12 H	0.12 H	0.12 H	0.12 H
p_2	b_2	0.14 B	0.24 B	0.30 B	0.29 B
	h_2	0.21 H	0.23 B	0.23 B	0.23 B
p_3	b_3	0.43 B	0.49 B	0.38 B	0.41 B
	h_3	0.36 H	0.35 H	0.32 H	0.30 H
Function Value					
ν_{yx}		6.04E-05	9.24E-06	4.70E-04	-1.84E-04
ν_{xy}		5.69E-05	-2.05E-03	1.96E-05	-1.53E-03
Mass (g)		9.42	9.33	8.91	8.89

The size ratio of the unit Fish-Cells to the overall size of the tessellation affects the structural behaviour of a metamaterial due to boundary condition effects like stress concentrations [18, 31]. Hence, a homogenisation study is conducted for an increasing number of tessellations where only odd numbers of tessellation sizes are considered to maintain symmetry along the longitudinal-y direction of the metamaterial. The homogenisation results are described in Appendix A. The optimised metamaterial shows convergence and homogeneity at a tessellation size of 21x21 for both longitudinal-y and transverse-x directions of loading. Thus, a tessellation size of 21x21 is used for any further discussions in this article. It must be noted that for section 5 and 7, the tessellation size had to be altered to meet the manufacturing and size constraint requirements, respectively.

4 Joint Design for Non-Linear Large Deformations, FE Modelling

4.1 FE Model Definitions

The parametric joint design study aims to sustain a consistent ZPR over a maximised strain range. Figure Fig. 5 illustrates the schematic of the optimised unit cell geometry with joints design parameters. Two unique parameters are considered as the joint length ratio (l/c) and the joint thickness ratios (t_2/t_1), where l is the local length of the joint, c is the length of the connector, t_1 is the global thickness of the unit cell members and t_2 is the local thickness of the unit cell members at the joints.

To study the effect of length ratio (l/c) on the optimised Fish-Cells metamaterial, three-length ratios (l/c) of 0.50, 0.75 and 0.90 are considered, while the thickness ratio is fixed as t_2/t_1= 0.50. The minimum value of the length ratio (l/c) is limited to 0.50 due to geometry overlap in connecting at joints 2 and 3, resulting in an undesired deformation mechanism. Investigating the effect of thickness ratio (t_2/t_1) on the optimised

Fish-Cells metamaterial, three (t_2/t_1) ratios of 0.25, 0.50 and 0.75 are considered with a fixed-length ratio as l/c = 0.50. The minimum thickness ratio (t_2/t_1) is limited to 0.25 due to computation time because of complex geometry and exceptionally fine meshing. About 5 million elements were required in the case of geometry with a thickness ratio of t_2/t_1= 0.25. Furthermore, the very thin joints impose challenges with regards to manufacturability and high-stress concentrations.

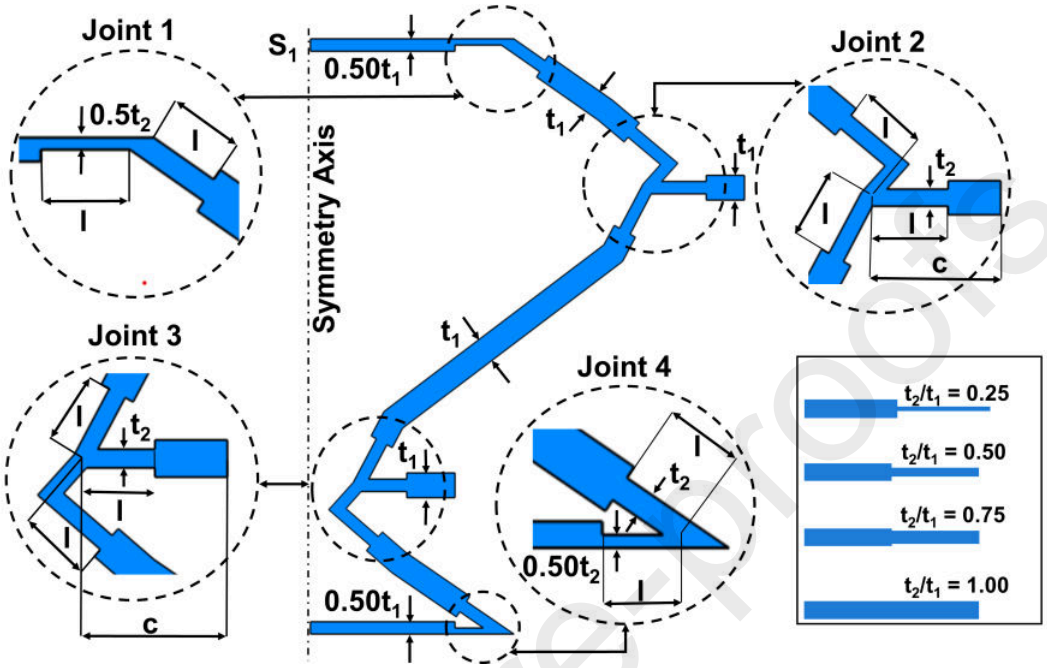

Fig. 5: Geometric definitions describing the dimension of the shape optimised Fish-Cells ZPR joints.

The material parameters and boundary conditions are adapted from section 2.1 and section 2.2 for FE simulations. A mesh convergence study is performed using quadratic plane stress (CPS8) elements due to its superior ability to capture complex stress formation at the joints relative to quadratic beam (B22) formulation [21]. A brief discussion describing the difference of the performance of Poisson's ratio and effective elastic modulus for the baseline metamaterial between B22 and CPS8 elements is provided in Appendix B. From the mesh convergence study, it is observed that Poisson's ratio of the metamaterial shows independence from the mesh size over large strain for a global mesh size of 0.20mm. Such a small element size is required to successfully capture the complex stress formation at the joints.

4.2 Results and Discussions

Fish-Cells metamaterial exhibits two unique deformation mechanisms for large strains under tensile loading in the longitudinal-y direction. The first mechanism corresponds to relative rotations at the joints and bending of slender elements of the unit cell. The second mechanism corresponds to the tensile stretching of the slender elements. Figure Fig. 6 illustrates the undeformed and deformed shapes of the central unit cell of the baseline metamaterial and optimised geometry with thickness ratios (t_2/t_1) of 1, 0.50 and 0.25 at strain showing the end of Mechanism I and the start of Mechanism II along with their corresponding maximum von mises stress values (σ_{max}). It is observed that the optimised (t_2/t_1 = 1) metamaterial shows a higher tendency of rotation at the joints relative to the baseline metamaterial. Similarly, with reducing thickness at the joints the optimised metamaterial shows higher tendency to rotate at the joints.

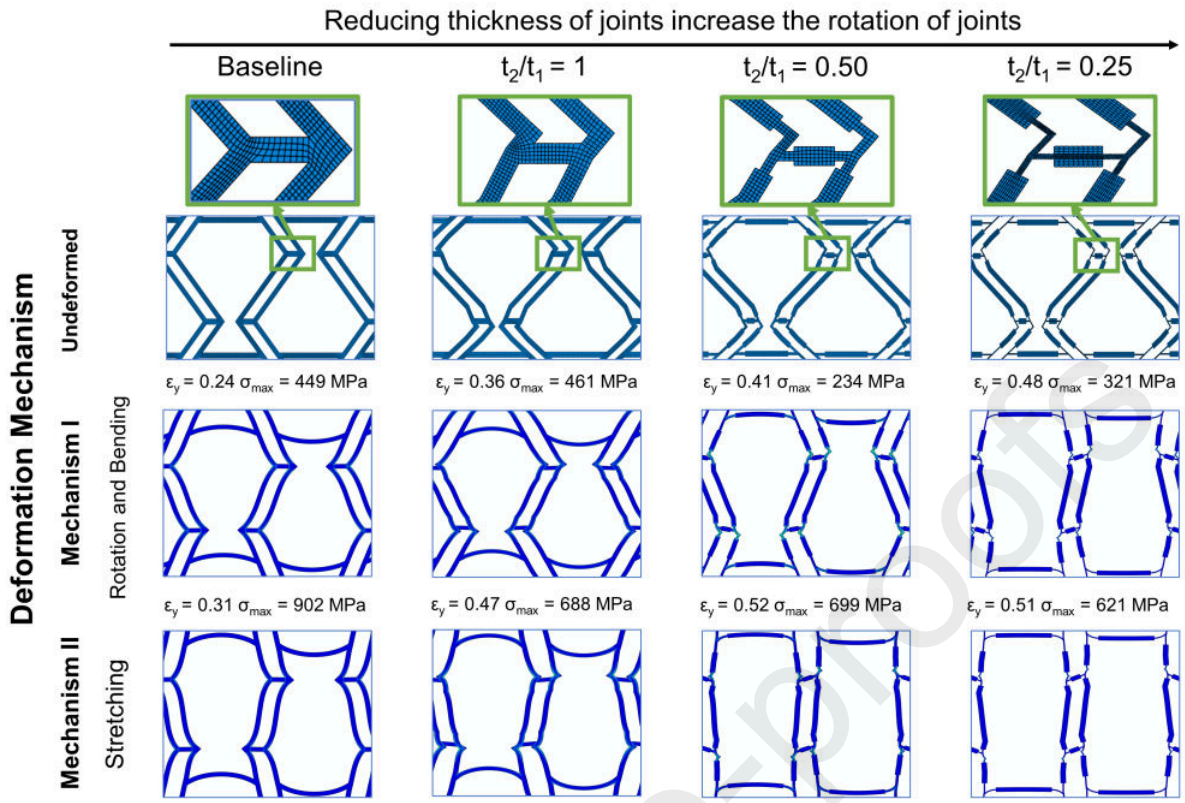

Fig. 6: Undeformed (along with mesh distribution at the joints) and deformed shapes of the central unit cell of the baseline and shape optimised Fish-Cells ZPR metamaterial with thickness ratios (t_2/t_1) of 1, 0.50 and 0.25 at strain showing the end of the deformation Mechanism I (joint rotation) and the start of deformation Mechanism II (stretching) along with their corresponding maximum von misses stress values (σ_{max}).

Figure Fig. 7a illustrates the variation of Poisson's ratio of the baseline metamaterial and the optimised geometry with different joint thickness under tensile strains in the longitudinal-y direction. The inflexion point of the Poisson's ratio curve corresponds to the strain which marks the end of Mechanism I and the start of Mechanism II.

Compared to baseline, the shape optimised metamaterial with uniform thickness t_2/t_1 = 1 shows better ZPR behaviour. For a strain of 1%, the optimised metamaterial shows 88.1 % lower absolute Poisson's ratio value relative to the baseline metamaterial. Similarly, a 25% lower maximum Poisson's ratio is observed at 46% higher maximum strain range for the optimised metamaterial compared to the baseline.

Reducing thickness at the joints of the optimised metamaterial:

- decrease the slope of the Poisson's ratio (ν_{yx}) with strain. An average slope of 0.119, 0.116, 0.042, 0.007 for the Poisson's ratio (ν_{yx}) is observed when considering a strain of up to 40%. Thus, with reducing thickness at the joints, the optimised metamaterial exhibits near-constant ZPR behaviour.
- causes a shift in the initial Poisson's ratio (ν_{yx}) in the positive y-axis. This effect seems to converge as the thickness ratio decreases and can be mitigated with joint optimisation using CPS8 element formulation using non-linear strain range but is not explored in this article due to the limitation of computational resources.
- shift the maximum value of the Poisson's ratio (ν_{yx}) towards a higher strain value. This signifies that the metamaterial with reduced thickness at the joints exhibits Mechanism I for a higher strain.

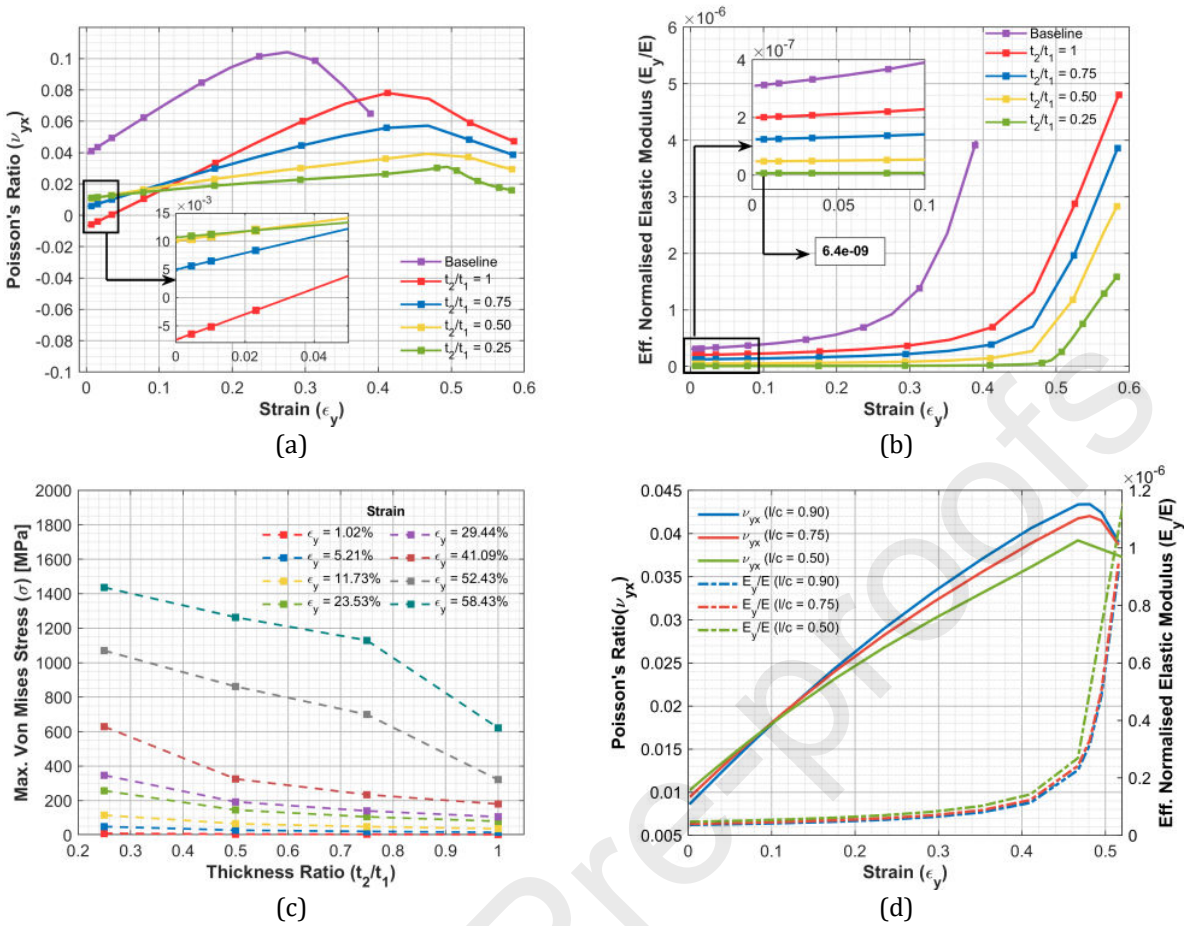

Fig. 7: Results obtained from the high fidelity FE analysis of the baseline and shape optimised Fish-Cells ZPR metamaterial (a) ν_{yx} v/s strain; (b) effective normalised elastic modulus (E_y/E) v/s strain baseline metamaterial and optimised metamaterial with varying thickness ratios (t_2/t_1); (c) maximum von misses stress (σ) with thickness ratios of the optimised metamaterial at different strain ranges under tensile load in the longitudinal-y direction and (d) ν_{yx} and E_y/E for varying length ratios.

It is observed that the Fish-Cell metamaterial exhibits Young's modulus values order of magnitudes smaller than its material of construction and hence, is suitable for low stiffness bio-medical applications. Figure Fig. 7b illustrates the variation of the effective normalised elastic modulus (E_y/E) for baseline and optimised ($t_2/t_1 = 1$) metamaterial, where the effective elastic modulus has been normalised with the elastic modulus of its original constituent material (PLA). The optimised ($t_2/t_1 = 1$) metamaterial is observed to be at least 33% less stiff compared to the baseline metamaterial. This gap only increases with increase in strain. The optimised metamaterial exhibits nearly constant stiffness up to the strain values which correspond to the inflexion point observed in Fig. 7a. With reducing thickness at the joints, the optimised metamaterial exhibits decreasing stiffness. For instance, the optimised ($t_2/t_1 = 0.25$) shows about 31 times lower stiffness compared to the optimised ($t_2/t_1 = 1$) metamaterial. So, due to improved stiffness characteristics of the optimised metamaterial throughout the strain range, relative to the baseline metamaterial, the optimised metamaterial fortifies its position as a superior candidate for morphing application.

For Fig. 7a and Fig. 7b, it must be noted that the maximum strain range is limited to approximately 58% due to high-stress values as illustrated in Fig. 7c. Also, Fig. 7c illustrates the variation of maximum von misses stress (σ_{max}) of the optimised metamaterial for different thickness ratios at varying strains. It is observed that the maximum stress increases with increasing strain and decreasing thickness at the joint. Additionally, the maximum strain range of the optimised metamaterial appears to be a function of the yield stress of the original constituent material. For instance, the maximum strain range of the optimised metamaterial ($t_2/t_1 = 0.25$) will be limited to approximately 7% when considering PLA (σ_y = 22 MPa), 41% strain when considering Aluminium 5083 H321 (σ_y = 220 MPa), 50% when considering Steel AISI 4130

(σ_y = 517 MPa) and up to 55% when considering Titanium AMS 4490 (σ_y = 1172 MPa) as materials of construction [30].

Figure Fig. 7d illustrates the variation of Poisson's ratio (ν_{yx}) and effective elastic modulus (E_y/E) for varying joint length ratios (l/c). It is observed that changing the length ratios did not yield a notable change in the slope of Poisson's ratio (ν_{yx}) and effective elastic modulus (E_y/E) of the optimised metamaterial. Thus, for optimised Fish-Cell metamaterial, the thickness ratio (t_2/t_1 = 1) seem to be the dominant parameters. Similar observations were recorded by Zhong et al. where they investigated the auxetic behaviour of tetra-chiral honeycomb structures and established a relationship between the deformation mechanism and its geometric parameters where they observed that by reducing the ligament length ratio (l/r), the slope of the Poisson's ratio curve leans towards ZPR behaviour. However, no such observation was made when the cell-wall thickness ratio (t/L) was altered [31].

The results for the parametric joint design study for tensile loading in the transverse-x direction is described in Appendix C. It is observed that for linear-elastic strain, the optimised metamaterial exhibits close to ideal ZPR behaviour when compared to the baseline metamaterial. But the general behaviour of the metamaterial, even with the varying thickness and length ratios, appears to be auxetic in nature. Also, the maximum strain range of the metamaterial appears to be limited to ~25% due to contact between adjacent members. This limits the application of the optimised Fish-Cells metamaterial to just one direction of loading for very large strain deformations.

From the discussions above, it is concluded that the optimised Fish Cells metamaterial with reduced joint thickness shows potential to be a viable candidate for ZPR morphing skins in the longitudinal-y direction.

5 Experimental Analysis

Validating numerical models, three geometries including baseline, optimised (t_2/t_1 = 1) and optimised with the reduced joint thickness (t_2/t_1 = 0.50) are manufactured and their force-displacement attributes are characterised experimentally under tensile loading in two orthogonal directions.

5.1 Geometries, Manufacturing Constraints and Experimental Setup

Six metamaterial samples are manufactured using a 3D printer (Ultimaker $^{2+}$) with Polylactic Acid (PLA). Manufactured samples include baseline, optimised (t_2/t_1 = 1) and optimised (t_2/t_1 = 0.50) metamaterials for longitudinal-y and transverse-x directions of tensile loading. The thickness ratio of 0.50 is considered due to the manufacturing limits of 3D printer. With regards to Fig. 7d, it is observed that for a length ratio ($\frac{l}{c}$) of 0.50 has least Poisson's ratio at max strain relative to the length ratio ($\frac{l}{c}$) of 0.75 and 0.90. Thus, the length ratio ($\frac{l}{c}$) of 0.50 was selected for the manufacturing process. Furthermore, two duplicates for each of the six samples are manufactured, bringing the total number of samples to 18. The data obtained from the experiments are averaged over the three identical samples.

The geometric parameters of the unit cell were changed and a tessellation size of 5x12 was selected; this is to obtain the maximum density of Fish-Cells for the available printing area (220 mm x 150 mm) in order to minimize the boundary condition effects. These updated parameters describing the locations of the basic and non-basic nodes are described in Table 5. It must be noted that the values for the non-basic nodes are in-coherent with the geometric definitions of the optimised (best compromise) unit cell geometry mentioned in Table 4 with the value of B/H ratio of 0.5.

A nozzle size of 0.25 mm was used to maximize the infill area and obtain an out-of-plane thickness of 1.5 mm for metamaterial skins. This thickness was a compromise between out-of-plane stiffness, ease of handling and manufacturing time. Each sample took approximately 12 hours to manufacture.

The experimental setup, as shown in Fig. 8 includes the metamaterial sample installed on the Instrom 5965 tensile test machine with a 5kN load cell along with the data acquisition system and a DSLR camera unit. The camera unit was used to capture images during the tensile test at an interval of 30 seconds. The force-displacement curves were recorded for a constant extension rate of 2mm/min until failure.

Table 5: Geometric parameters of the shape optimised Fish-Cells ZPR metamaterial used in experimental validations.

	Parameters	Dimensions [mm]
Basic	B	8
	H	16
	b	3
	h	3
	c	2
	t	1
Non- Basic	p_1	b_1 2.35
		h_1 1.92
	p_2	b_2 0.70
		h_2 3.36
	p_3	b_3 1.78
		h_3 5.76

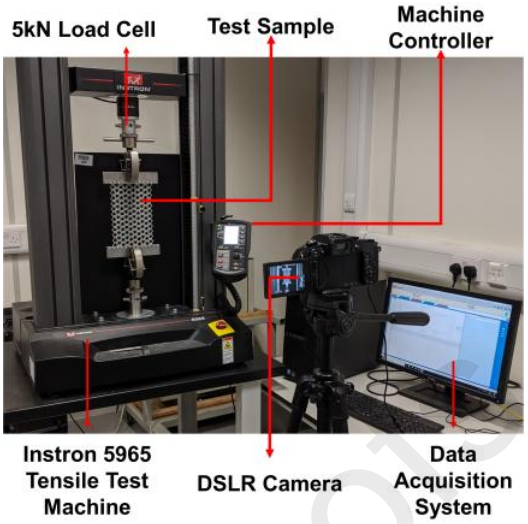

Fig. 8: Data acquisition system with the tensile test machine and image recording system.

5.2 Experimental and Numerical Result Comparison

In this section, numerical models were generated using: material properties described in section 2.1; boundary conditions described in section 2.2; mesh definitions described in section 4.1 and geometric properties described in Table 5. Figure 10a shows the force-displacement graphs for the numerical and experimental models with a very good correlation.

The experiments demonstrated in Fig.9 shows improved ranges for ZPR strains in longitudinal-y direction samples. The shape optimized samples with uniform thickness and reduced joint thickness show 1.44 and 2.44 times larger strains respectively in compare to Fish-Cells Baseline. However, the ZPR strain range in transverse-x direction was not improved. Figure Fig. 9 illustrates the deformed test samples under tensile loading at their respective failure strain. In addition, five dog bone test sample in section 2.1 were manufactured using the same spool of material for consistency in material characterisation.

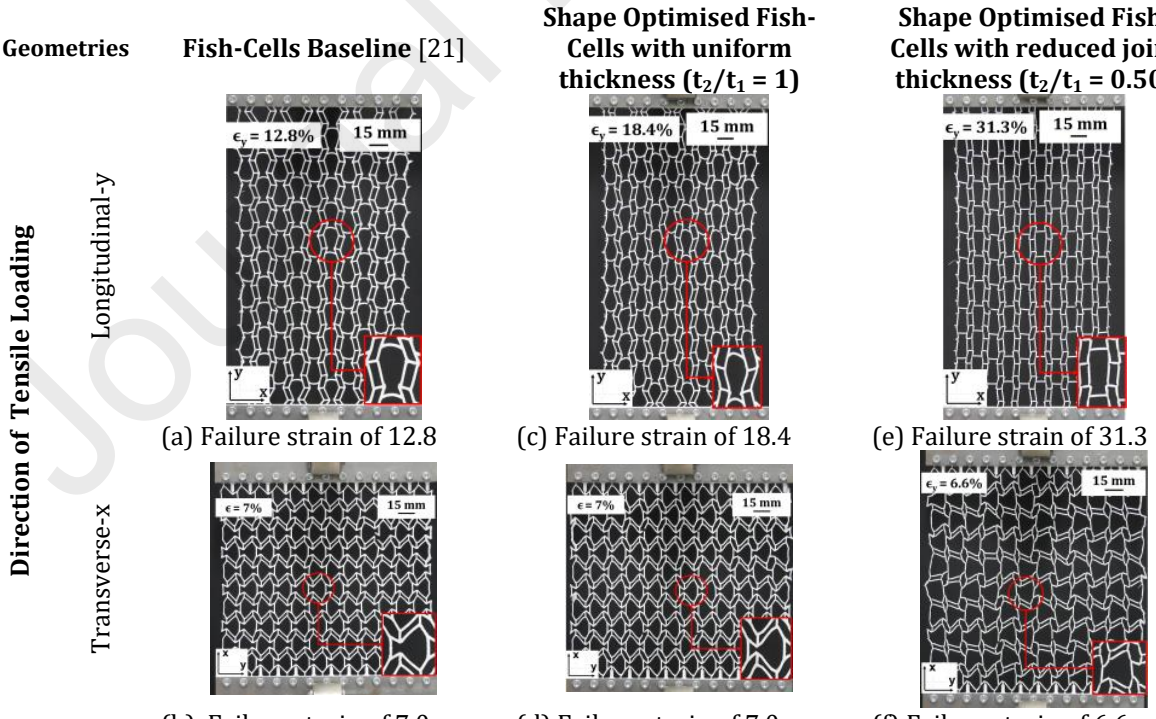

(a) Failure strain of 12.8 (c) Failure strain of 18.4 (e) Failure strain of 31.3

(b) Failure strain of 7.0 (d) Failure strain of 7.0 (f) Failure strain of 6.6

Fig. 9: Experimental comparison of failure strains corresponding to Baseline and Shape optimised Fish-Cells ZPR metamaterials.

Figure Fig. 10b describes in-plane stiffness for the six test samples. The effective in-plane stiffness of the test samples is calculated by measuring the slope within the linear region of the force-displacement curves. It is observed that for tensile loading in the transverse-x direction, the optimised metamaterial with uniform thickness (t_2/t_1 = 1) and reduced joint thickness (t_2/t_1 = 0.50) have reduced stiffness by 8.7% and 76.3% respectively when compared to baseline Fish-Cells stiffness of 20.7 N/mm. Similarly, for the longitudinal-y direction, the optimised shape with uniform thickness (t_2/t_1 = 1) and with reduced joint (t_2/t_1 = 0.50) have lowered stiffness by 28.9% and 80% respectively, when compared to baseline samples with a stiffness of 4.5 N/mm.

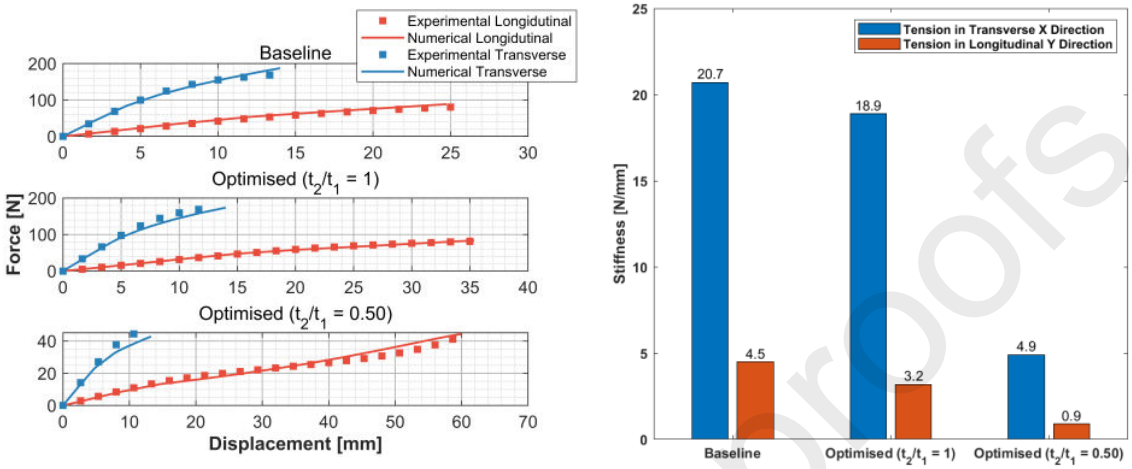

(a) (b)

Fig. 10: Results obtained from experimental analysis (a) comparative force-displacement plots of the numerical and experimental analysis and (b) Bar plots illustrating the effective tensile stiffness for the baseline Fish-Cells ZPR metamaterial, shape optimised Fish-Cells ZPR with uniform thickness (t_2/t_1 =1) and shape optimised Fish-Cells ZPR metamaterial with a reduced joint thickness (t_2/t_1 =0.50) in the linear-elastic strain range.

6 Linear Buckling Analysis

The effect of shape optimisation and joint design on tensile behaviour of the Fish-Cells ZPR metamaterial was discussed in the previous section. However, the in-plane compressive behaviour must also be considered especially for morphing skins applications [32]. Hence, a FE linear buckling analysis is devised to study the buckling performance of the baseline and shape optimised Fish-Cells ZPR metamaterials.

The geometric parameters presented in Table 2 and Table 4 were used for buckling analysis of the baseline Fish-Cells and shape optimised geometries with thickness ratio (t_2/t_1) of 1, 0.50 and 0.25. The boundary conditions defined for the buckling analysis are described in Table 6 with edge numbers defined in Fig. 3. A distributed compressive load of 1 N/mm was applied to a reference node which was tied to the shell edge using rigid 1D beam elements (MPC). A homogenised tessellation size of 21x21 with elastic properties of PLA presented in Table 1 was used for this analysis. These models were discretised by a global mesh size of 0.20 and four-node, quadrilateral shell elements with reduced integration (S4R). An equivalent plate with identical dimensions was considered for comparison as shown in Fig. 11 [23].

Figure Fig. 11 illustrates the first buckling mode shape of the shape optimised Fish-Cells with uniform thickness (t_2/t_1 = 1) and the equivalent orthotropic plate for both orthogonal directions. It is observed that the equivalent plate, the baseline, and shape optimised Fish-Cells with thickness ratios of 1, 0.5 and 0.25 tend to have identical mode shapes in both directions of loading, respectively. Results show a critical buckling load of 71.77 N and 14.40 N for the equivalent plate in transverse-x and longitudinal-y directions. The critical buckling load for the Baseline and shape optimized Fish-Cells metamaterials are normalised with respect to the equivalent plate, as presented in Table 7.

Table 6: Boundary conditions for buckling analysis of Fish-Cells ZPR metamaterials.

Direction of Compressive Loading					
Longitudinal y			**Transverse x**		
Edge Number	1 & 3	Free	**Edge Number**	2 & 4	Free
	2	$\varepsilon_x = 0$ ε_y = Free $\varepsilon_z = 0$ $UR_1 = 0$ $UR_2 = 0$ $UR_3 = 0$		1	$\varepsilon_x = 0$ $\varepsilon_y = 0$ $\varepsilon_z = 0$ $UR_1 = 0$ $UR_2 = 0$ $UR_3 = 0$
	4	$\varepsilon_x = 0$ $\varepsilon_y = 0$ $\varepsilon_z = 0$ $UR_1 = 0$ $UR_2 = 0$ $UR_3 = 0$		3	ε_x = Free $\varepsilon_y = 0$ $\varepsilon_z = 0$ $UR_1 = 0$ $UR_2 = 0$ $UR_3 = 0$

Table 7: Normalised buckling load for Fish-Cells ZPR metamaterials.

Normalised Buckling Load		
Geometry	**Loading Direction**	
	Longitudinal y	**Transverse x**
Plate	1	1
Baseline	0.03813	0.02853
Optimised (t_2/t_1=1)	0.03196	0.03185
Optimised (t_2/t_1= 0.50)	0.01122	0.01334
Optimised (t_2/t_1=0.25)	0.00346	0.00487

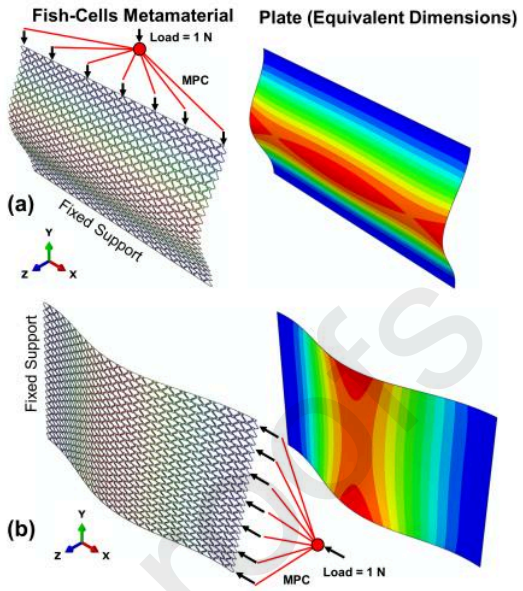

Fig. 11: First buckling mode for the Shape Optimised Fish-Cells ZPR metamaterial and the equivalent plate of identical dimensions under compressive load in (a) longitudinal-y direction and (b) transverse-x direction.

The shape optimised Fish-Cells with uniform thickness is 16.2% less stiff and 11.6% stiffer compared to the baseline Fish-Cells in the longitudinal-y and transverse-x directions, respectively. Both baseline and shape optimised Fish-Cells metamaterial show 97% lower buckling load compared to the equivalent plate in both directions. Also, it is observed that with decreasing thickness ratios (t_2/t_1), the critical buckling load decreases, highlighting the compromise between large strains ZPR and buckling capacity.

7 Morphing Wing Application of Large Strain ZPR Fish-Cells Metamaterial

Realizing the mechanical behaviour of shape optimised Fish-Cells ZPR metamaterial in tension and compression, a preliminary design study is performed to assess the structural integrity of this large strain ZPR metamaterial as a candidate for morphing skin. The structure of the morphing wing is based on the Fish-Bone Active Camber concept introduced by Woods et al. [33].

It should be noted that the design of a morphing wing is not a trivial process and may require fluid-structure interaction analysis, particularly if unsteady effects are considered. In practice, the morphing skin would be optimised simultaneously with the internal supporting structure to achieve the highest possible lift to drag ratio. This can be achieved by considering an equivalent skin model to capture the actuator force required to deform the skin. The predicted aerodynamic pressure allows the out-of-plane deformations of the skin to be estimated, and these deformations are constrained so that their effect on the aerodynamics, particularly drag is negligible. Other constraints may be added, based on manufacturing requirements like number and distance between stringer pairs, length of morphing section, structural integrity, and fatigue. Also, the optimum skin would be different if more importance is given to a certain objective function such as the flexibility of the whole structure, which reduces the required energy to morph resulting in a lighter actuation system [25]. Such optimization is beyond the scope of this article, although, a FE simulation of the skin and internal structure under typical aerodynamic and structural loadings is performed to verify the design approach.

7.1 FE Modelling

This section provides details of the geometry of the wing assembly, dimensions of the optimised Fish-Cells metamaterial, mesh definitions, boundary conditions and material properties used for the numerical modelling of the morphing wing with ZPR skin.

Figure Fig. 12 illustrates the proposed camber morphing wing assembly along with its constituent parts. A 3D surface geometry is generated using NACA 0012 airfoil [34]. The wing assembly constitutes a supporting internal structure and a morphing sandwich skin. The supporting structure constitutes a rigid leading and trailing edge along with deformable spine and stingers. The morphing sandwich skin constitutes of the optimised Fish-Cells ZPR metamaterial tied to the exterior elastomer using node-to-surface contact discretisation technique. The supporting and the morphing skin are then tied to the rigid leading and trailing edge using surface-to-surface contact discretisation technique. The leading edge, trailing edge, spine, stringer, metamaterial, and elastomers are generated as 3D shell extrude features. Shell elements are considered to avoid the complexity of 3D solid elements and to keep the computation time in check. The geometry, mesh and material definitions of the morphing wing assembly are described in Appendix D.

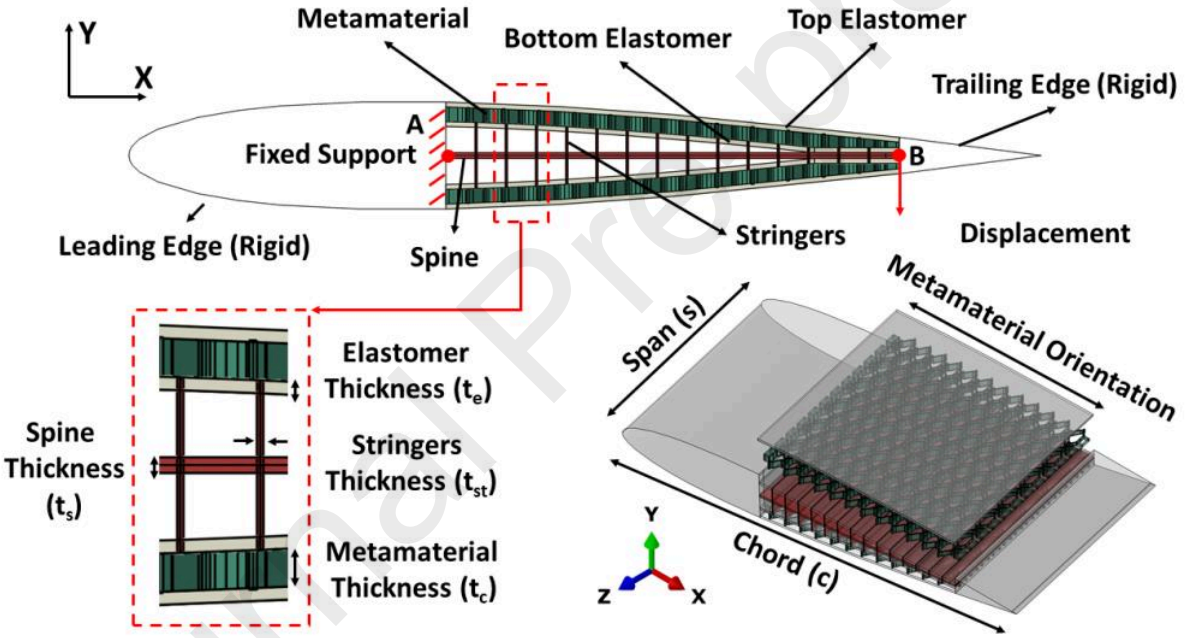

Fig. 12: Morphing wing assembly with Fish-Cell ZPR skin and boundary conditions.

To obtain the geometry of the unit cell for the metamaterial panel, the dimension of the basic and the non-basic nodes (defined in Table 2 and Table 4) are scaled-down by 50% to maintain a B/H ratio of 0.33. The metamaterial panel consists of 6-unit cells in spanwise and 12-unit cells in the chordwise directions. Three different thickness of 1mm, 2mm and 5mm for the sandwich skin are considered. For the boundary condition, the rigid leading-edge is fixed at Point A and displacement of 25mm is applied to the rigid trailing edge at Point B in the negative y-direction, as shown in Fig. 12.

7.2 FE Wing Morphing Results

Figure Fig. 13a illustrates the force-displacement characteristics of the morphing wing assembly with metamaterial thickness (t_c) of 1mm, 2mm and 5mm. The results show that the out-of-plane bending stiffness of the wing assembly increases with increasing the metamaterial thickness. It is observed that relative to the out-of-plane stiffness of 1.76 N/mm for the metamaterial thickness of 1 mm, the panel with 2 mm and 5 mm thickness has 27.3% and 36.4% higher out-of-plane bending stiffness. Thus, the actuation force increases with the increasing metamaterial panel thickness. Also, only a 7% increase in the stiffness is observed for the metamaterial thickness (t_c) of 5 mm as compared to 2 mm. Therefore, the relative

difference in the stiffness of the metamaterial diminishes and the total mass of the assembly increases with increasing metamaterial thickness (t_c). This calls for an optimisation study to obtain the best compromise between the in-plane stiffness for lower actuation force, flexural stiffness (for higher aerodynamic load carrying capacity) and mass, similar to one conducted by Dayyani et al. [24], which can be explored in a future study.

Furthermore, Fig. 13b illustrates the buckling performance of the sandwich panel of the morphing wing assembly. For a metamaterial thickness (t_c =1 mm), both local buckling of the elastomer skin and global buckling of the metamaterial is observed. On the contrary, for a metamaterial thickness (t_c =5 mm), only local buckling of the elastomer skin is observed. Therefore, the global buckling of the metamaterial can be mitigated by using a higher thickness. Also, the local buckling of the elastomer skin can be mitigated using pre-stressed elastomeric coating which may be investigated in a future detailed design study.

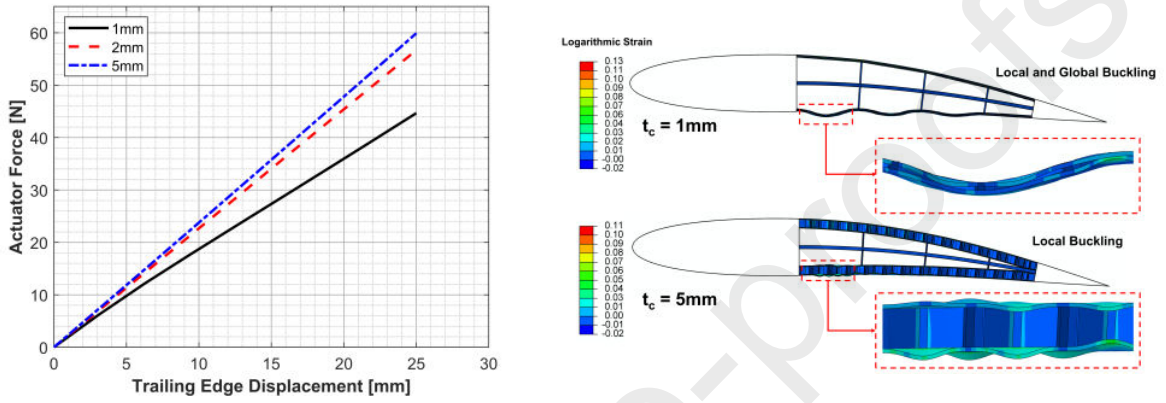

(a) (b)

Fig. 13: (a) Actuator force vs trailing edge displacement for morphing wing assembly for 1mm (black), 2mm (red) and 5mm (blue) metamaterial panel width; (b) Logarithmic strain contours for morphed wing structure with 25 mm displacement for metamaterial panel width of (a) 1 mm and (b) 5 mm.

8 Conclusions

Genetic algorithm shape optimisation is performed on the baseline Fish-Cells metamaterial to improve its ZPR characteristics in the linear-elastic strain range. Four sets of unit Fish-Cells parameters are summarised for the shapes including the best ν_{yx}, best ν_{xy}, best mass, and the best compromise. The ZPR and effective elastic modulus characteristics of the metamaterial with the best compromise shape was compared to the baseline metamaterial using high fidelity large deformation FE analysis for homogenised tessellation size of 21x21 under tensile loading for both directions of loading. It was observed under tensile loading in longitudinal-y direction, for a strain of 1%, the optimised metamaterial shows 88.1 % lower absolute Poisson's ratio value relative to the baseline metamaterial. Similarly, a 25% lower maximum Poisson's ratio is observed at 46% higher maximum strain range for the optimised metamaterial compared to the baseline. Also, the optimised (t_2/t_1 = 1) metamaterial is observed to be at least 33% less stiff compared to the baseline metamaterial.

To obtain a consistent ZPR behaviour over a maximised strain range, a joint design parametric study is devised using three unique joint length and joint thickness ratios. It is observed that for reducing thickness at the joints, increased maximum strain range and lower overall Poisson's ratio. The shape optimised metamaterial with a thickness ratio of 0.25, relative to the baseline Fish-Cells metamaterial shows 70% lower poison's ratio in the longitudinal-y direction at 75% higher strain.

Furthermore, it is observed that the maximum strain range of the Fish-Cells metamaterial is dependent on the yield stress of the original constituent material. For example, the maximum strain range of the Fish-Cells metamaterial will only be limited to 7% when the constituent material is PLA and 55% when the constituent material is Titanium AMS 4490 before the material yields.

In order to understand the behaviour of the Fish-Cells metamaterial under compressive loading, a linear eigenvalue buckling analysis is performed and its buckling load in compared to a plate of identical dimensions. It is observed that the baseline and shape optimised Fish-Cells metamaterial show 97% lower critical buckling load compared to the equivalent plate of identical dimensions. Furthermore, decreasing thickness ratios (t_2/t_1), the critical buckling load decreases, highlighting the compromise between large strains ZPR and buckling capacity.

Realizing the mechanical behaviour of shape optimised Fish-Cells ZPR metamaterial in tension and compression, a preliminary design study is performed to assess the structural integrity of this large strain ZPR metamaterial as a candidate for morphing skin. In conclusion, the optimised Fish-Cells metamaterial with reduced thickness at the joint show potential for large strain ZPR morphing application.

References

[1] S. Vasista, O. Mierheim, M. Kintscher, Morphing Structures, Applications of, in: H. Altenbach, A. Öchsner (Eds.), Encycl. Contin. Mech., Springer Berlin Heidelberg, Berlin, Heidelberg, 2019: pp. 1–13. https://doi.org/10.1007/978-3-662-53605-6_247-1.

[2] S. Barbarino, O. Bilgen, R.M. Ajaj, M.I. Friswell, D.J. Inman, A review of morphing aircraft, J. Intell. Mater. Syst. Struct. 22 (2011) 823–877. https://doi.org/https://doi.org/10.1177/1045389X11414084.

[3] N.G. Ozdemir, F. Scarpa, M. Craciun, C. Remillat, C. Lira, Y. Jagessur, L. Da Rocha-Schmidt, Morphing nacelle inlet lip with pneumatic actuators and a flexible nano composite sandwich panel, Smart Mater. Struct. 24 (2015). https://doi.org/10.1088/0964-1726/24/12/125018.

[4] S. Daynes, P.M. Weaver, Review of shape-morphing automobile structures: Concepts and outlook, Proc. Inst. Mech. Eng. Part D J. Automob. Eng. 227 (2013) 1603–1622. https://doi.org/10.1177/0954407013496557.

[5] X. Lachenal, S. Daynes, P.M. Weaver, Review of morphing concepts and materials for wind turbine blade applications, Wind Energy. 16 (2013) 283–307. https://doi.org/10.1002/we.531.

[6] I.P.S. Qamar, R. Groh, D. Holman, A. Roudaut, HCI meets material science: A literature review of morphing materials for the design of shape-changing interfaces, in: Conf. Hum. Factors Comput. Syst. - Proc., ACM Press, New York, New York, USA, 2018: pp. 1–23. https://doi.org/10.1145/3173574.3173948.

[7] S.H. Ahn, K.T. Lee, H.J. Kim, R. Wu, J.S. Kim, S.H. Song, Smart Soft Composite: An Integrated 3D Soft Morphing Structure Using Bend-twist Coupling of Anisotropic Materials, Int. J. Precis. Eng. Manuf. 13 (2012) 631–634. https://doi.org/10.1007/s12541-012-0081-8.

[8] K.J. Cho, J.S. Koh, S. Kim, W.S. Chu, Y. Hong, S.H. Ahn, Review of manufacturing processes for soft biomimetic robots, Int. J. Precis. Eng. Manuf. 10 (2009) 171–181. https://doi.org/10.1007/s12541-009-0064-6.

[9] K. Bertoldi, V. Vitelli, J. Christensen, M. van Hecke, Flexible mechanical metamaterials, Nat. Rev. Mater. 2 (2017) 17066. https://doi.org/10.1038/natrevmats.2017.66.

[10] H.M.A. Kolken, A.A. Zadpoor, Auxetic mechanical metamaterials, RSC Adv. 7 (2017) 5111–5129. https://doi.org/10.1039/c6ra27333e.

[11] J.N. Grima, L. Oliveri, D. Attard, B. Ellul, R. Gatt, G. Cicala, G. Recca, Hexagonal Honeycombs with Zero Poisson's Ratios and Enhanced Stiffness, Adv. Eng. Mater. 12 (2010) 855–862. https://doi.org/10.1002/adem.201000140.

[12] C. Yang, H.D. Vora, Y. Chang, Behavior of auxetic structures under compression and impact forces, Smart Mater. Struct. 27 (2018) 025012. https://doi.org/10.1088/1361-665X/aaa3cf.

[13] M. Sanami, N. Ravirala, K. Alderson, A. Alderson, Auxetic materials for sports applications, in: Procedia Eng., 2014: pp. 453–458. https://doi.org/10.1016/j.proeng.2014.06.079.

[14] W. Ren, P.J. McMullan, A.C. Griffin, Poisson's Ratio of Monodomain Liquid Crystalline Elastomers, Macromol. Chem. Phys. 209 (2008) 1896–1899. https://doi.org/10.1002/macp.200800265.

[15] J. Liu, Y. Zhang, A Mechanics Model of Soft Network Materials With Periodic Lattices of Arbitrarily Shaped Filamentary Microstructures for Tunable Poisson's Ratios, J. Appl. Mech. 85 (2018) 051003. https://doi.org/10.1115/1.4039374.

[16] H. Yang, L. Ma, Multi-stable mechanical metamaterials with shape-reconfiguration and zero Poisson's ratio, Mater. Des. 152 (2018) 181–190. https://doi.org/10.1016/j.matdes.2018.04.064.

[17] K. Wang, Y.-H. Chang, Y. Chen, C. Zhang, B. Wang, Designable dual-material auxetic metamaterials using three-dimensional printing, Mater. Des. 67 (2015) 159–164. https://doi.org/10.1016/j.matdes.2014.11.033.

[18] J. Liu, Y. Zhang, Soft network materials with isotropic negative Poisson's ratios over large strains,

Soft Matter. 14 (2018) 693–703. https://doi.org/10.1039/C7SM02052J.

[19] A. Clausen, F. Wang, J.S. Jensen, O. Sigmund, J.A. Lewis, Topology Optimized Architectures with Programmable Poisson's Ratio over Large Deformations, Adv. Mater. 27 (2015) 5523–5527. https://doi.org/10.1002/adma.201502485.

[20] Z. Ge, H. Hu, Y. Liu, A finite element analysis of a 3D auxetic textile structure for composite reinforcement, Smart Mater. Struct. 22 (2013) 084005. https://doi.org/10.1088/0964-1726/22/8/084005.

[21] M. Naghavi Zadeh, I. Dayyani, M. Yasaee, Fish Cells, a new zero Poisson's ratio metamaterial—Part I: Design and experiment, J. Intell. Mater. Syst. Struct. 31 (2020) 1617–1637. https://doi.org/10.1177/1045389X20930079.

[22] M.N. Zadeh, I. Dayyani, M. Yasaee, Fish Cell , a New Zero Poisson ' s Ratio Metamaterial . Part II : Elastic Properties, Under Rev. (2020) 1–24. https://doi.org/10.1177/1045389X20930079.

[23] M.N. Zadeh, I. Dayyani, M. Yasaee, Fish Cells, a new zero Poisson's ratio metamaterial—part II: Elastic properties, J. Intell. Mater. Syst. Struct. 31 (2020) 2196–2210. https://doi.org/10.1177/1045389X20942576.

[24] I. Dayyani, H.H. Khodaparast, B.K.S. Woods, M.I. Friswell, The design of a coated composite corrugated skin for the camber morphing airfoil, J. Intell. Mater. Syst. Struct. 26 (2015) 1592–1608. https://doi.org/10.1177/1045389X14544151.

[25] I. Dayyani, M.I. Friswell, Multi-objective optimization for the geometry of trapezoidal corrugated morphing skins, Struct. Multidiscip. Optim. 55 (2017) 331–345. https://doi.org/10.1007/s00158-016-1476-4.

[26] A. Ermakova, I. Dayyani, Shape optimisation of composite corrugated morphing skins, Compos. Part B Eng. 115 (2017) 87–101. https://doi.org/10.1016/j.compositesb.2016.10.029.

[27] J. Lim, C. You, I. Dayyani, Multi-objective topology optimization and structural analysis of periodic spaceframe structures, Mater. Des. 190 (2020) 108552. https://doi.org/10.1016/j.matdes.2020.108552.

[28] R.T. Marler, J.S. Arora, Survey of multi-objective optimization methods for engineering, Struct. Multidiscip. Optim. 26 (2004) 369–395. https://doi.org/10.1007/s00158-003-0368-6.

[29] I. Dayyani, B.K.S. Woods, M.I. Friswell, H.H. Khodaparast, The Optimal Design of a Coated Corrugated Skin for the FishBAC Morphing Wing, 24th Int. Conf. Adapt. Struct. Technol. (2013) 1–11. https://pdfs.semanticscholar.org/1439/65801229276cf7120d8423dc96518e87eba7.pdf.

[30] R.C. Rice, J.L. Jackson, J. Bakuckas, S. Thompson, Metallic materials properties development and standardization, MMPDS). Natl. Tech. Inf. Serv. Cap. (2003) 1–4.

[31] R. Zhong, M. Fu, Q. Yin, O. Xu, L. Hu, Special characteristics of tetrachiral honeycombs under large deformation, Int. J. Solids Struct. 169 (2019) 166–176. https://doi.org/10.1016/j.ijsolstr.2019.04.020.

[32] A.D. Shaw, I. Dayyani, M.I. Friswell, Optimisation of composite corrugated skins for buckling in morphing aircraft, Compos. Struct. 119 (2015) 227–237. https://doi.org/10.1016/j.compstruct.2014.09.001.

[33] B.K.S. Woods, M.I. Friswell, Preliminary Investigation of a Fishbone Active Camber Concept, in: Vol. 2 Mech. Behav. Act. Mater. Integr. Syst. Des. Implementation; Bio-Inspired Mater. Syst. Energy Harvest., American Society of Mechanical Engineers, 2012: pp. 555–563. https://doi.org/10.1115/SMASIS2012-8058.

[34] I.-C. Chang, F.J. Torres, C. Tung, Geometric analysis of wing sections, NASA Tech. Memo. 110346. (1995). https://ntrs.nasa.gov/search.jsp?R=19950018209 (accessed January 28, 2020).

Appendix A

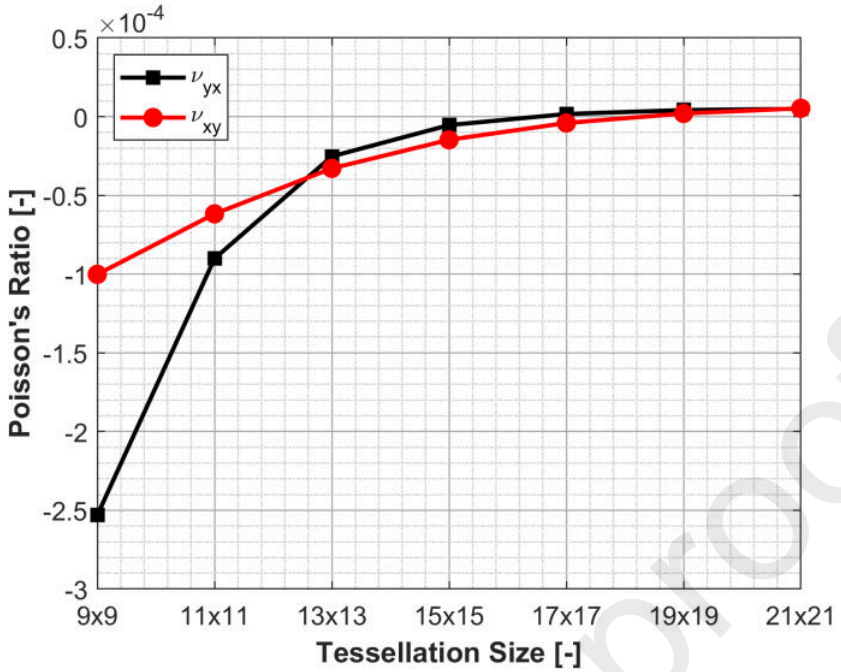

Fig. A: Convergence of Poisson's ratio in longitudinal-y (ν_{yx}) and transverse-x (ν_{xy}) direction of tensile loading.

Appendix B

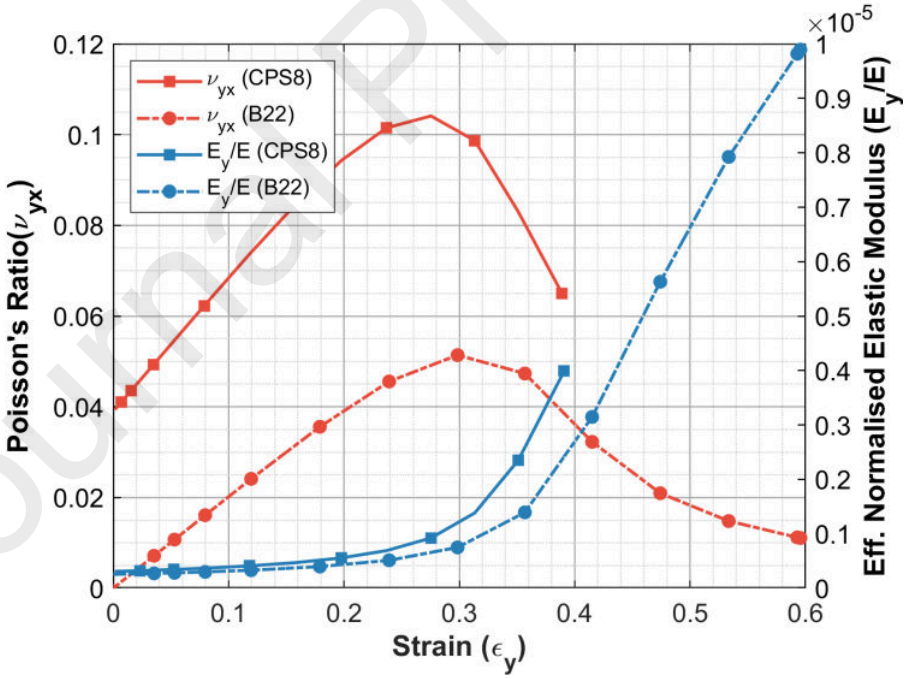

Fig. B: Comparison of Poisson's ratio (ν_{yx}) and effective elastic modulus (Ey/E) of the baseline metamaterial with strain for quadratic beam (B22) and plane stress (CPS8) element formulation under the longitudinal-y direction of tensile strain.

Appendix C

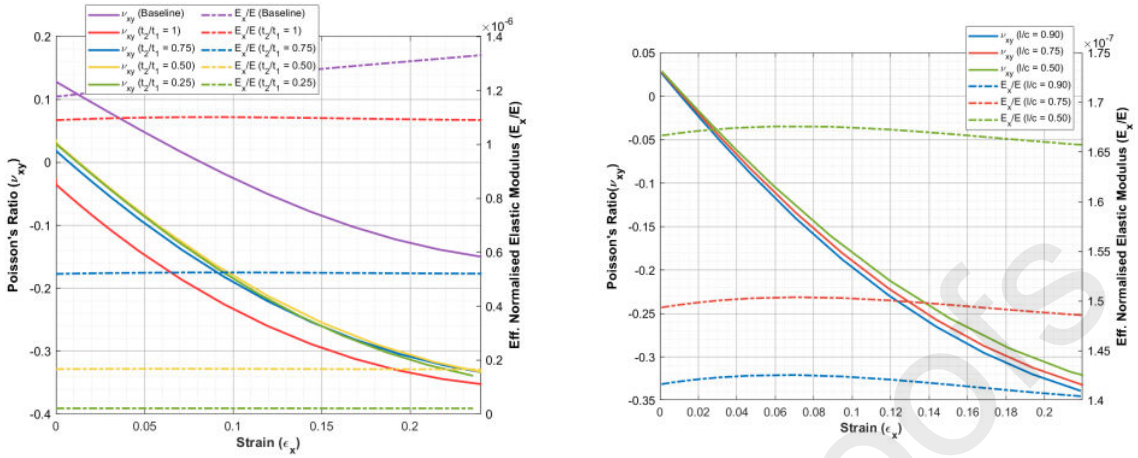

(a) (b)

Fig. C: Poisson's ratio (ν_{xy}) and effective elastic modulus (E_x/E) of the baseline metamaterial and the optimised geometry with varying (a) thickness ratios (t_2/t_1) and (b) length ratios (l/c) in the transverse-x direction of tensile strain.

Appendix D

Table D1: Mesh definitions for morphing wing assembly.

Geometry	Mesh Type	Mesh Size [mm]
Elastomer	S4R	0.50
Metamaterial Core	S4R	1
Leading-Edge	R3D4 (Rigid)	1
Trailing-Edge	R3D4(Rigid)	0.50
Spine and Stringers Pairs	S4R	0.50

Table D2: Geometry definitions of the morphing wing supporting structure.

Air-Foil Geometric Parameters	Value (Units)
Chord (c)	305 mm
Span (s)	150 mm
Start of Morphing Skin (x_s)	0.35c = 107 mm
End of Morphing Skin (x_e)	0.85c = 260 mm
Spine Thickness (t_s)	2 mm
Stringer Thickness (t_{st})	0.8 mm
No. of Stringer Pairs	3
Elastomer Thickness (t_e)	0.5 mm

Table D3: Material definitions for morphing wing assembly.

Material	Elastic Modulus (E) [MPa]	Poisson's ratio (ν)
Acrylonitrile Butadiene Styrene (ABS)	2140	0.3
Glass Fibre (Equivalent Isotropic)	33473	0.21
Elastomer Skin	10	0.48

Data Statement

The raw/processed data required to reproduce these findings cannot be shared at this time due to technical limitations and can be made available on request by the corresponding author, Dr Iman Dayyani.

Shape optimisation and buckling analysis of large strain Zero Poisson's Ratio fish-cells metamaterial for morphing structures

Jha, Ashutosh

2021-04-17

Jha A, Dayyani I. (2021) Shape optimisation and buckling analysis of large strain Zero Poisson's Ratio fish-cells metamaterial for morphing structures. Composite Structures, Volume 268, July 2021, Article number 113995

https://doi.org/10.1016/j.compstruct.2021.113995